J. Fluid Mech. (1992), *vol.* 234, *pp.* 529–552
Printed in Great Britain

Spin-down to rest in a cylindrical cavity

By Ö. SAVAŞ†
School of Aerospace and Mechanical Engineering, The University of Oklahoma, Norman, OK 73019, USA

(Received 10 November 1990 and in revised form 28 June 1991)

The nature of the flow during impulsive spin-down to rest in a cylindrical cavity is studied experimentally. Flow visualization using reflective flakes and laser-Doppler velocimetry are the tools of this investigation. The velocimeter is configured to measure simultaneously the azimuthal velocity component at two arbitrarily separated locations within the cylinder. The Ekman number is about 10^{-5} and the flow is unstable. The mean angular velocity decreases non-uniformly and monotonically. The velocity fluctuation amplitudes and frequencies decrease steadily. A novel data analysis is used to study the velocity fluctuations, which are neither stationary nor uniform. The assumptions of this analysis are the validity of Taylor's hypothesis of frozen-eddy transport and the ergodicity of the process following that rescaling. The fluctuations are equally dominant during all phases of the spin-down process when scaled with the current mean velocity. The root-mean-squared intensity measurements in the *core* ($r/R < 0.4$) suggest an r^{-1} dependence while a uniform value is observed in the *buffer* region ($0.4 < r/R < 0.8$). Flow visualizations and spatial velocity correlations indicate that the flow in the core consists of vortices having axes parallel to the rotation axis and extending throughout the height of the cylinder. The power spectra of the velocity fluctuations, after amplitude scaling with the current mean velocity and Taylor's scaling in time, suggest a -2.6 power dependence on the wavenumber k. The flow in the latter phases tends to a single vortex.

1. Introduction

1.1. *General remarks*

The flow field of concentrated vorticity in a viscous fluid is characterized by a global rotation and a finer scale turbulence riding on it if the Reynolds number is sufficiently high. An important question is how the turbulence and the mean flow interact. If we start from the hypothesis that large eddies are also slow dissipation engines, then the question of interaction can be more precisely stated. As the mean flow slows down, how does the turbulence accommodate itself to the varying flow conditions? Can viscosity dissipate energy fast enough so that the remaining turbulence is in equilibrium with the mean flow? If there exists a critical condition separating a regime where the turbulence cannot be accommodated by the mean flow, then how is the excess energy handled? In particular, is the energy expelled from the domain or is it lumped into vortical islands within the flow field? We might be at a disadvantage in seeking answers to these questions through studies of natural phenomena for those flows are likely to be in equilibrium. We must disturb those

† Permanent address: Department of Mechanical Engineering, University of California, Berkeley, CA 94720, USA.

equilibria and observe the subsequent behaviour to look for answers. Nevertheless, there are some naturally occurring *transient* phenomena that are likely to present opportunities for studies of the interaction between the mean flow and the turbulence. In this category we may list intense atmospheric vortices where disturbances brought about by local phenomena give rise to such transient vortices. Along these lines, Scorer (1966) proposes that a rotating fluid mass should tend to a concentrated vortex if stirred. Gough & Lynden-Bell (1968) found evidence supporting Scorer's hypothesis while, at the same time, Bretherton & Turner (1968) argue that there is no clear evidence either for or against it. Ibbetson & Tritton (1975) and Hopfinger, Browand & Gagne (1982) discuss two experiments on turbulence in rotating flows.

Ibbetson & Tritton's (1975) experiment is on the effect of rotation on decaying turbulence. Conclusions from the experiment are that rotation increases the decay rate of the turbulence in general and that the probable mechanism is the transfer of energy by inertial waves to the walls where it is dissipated in viscous boundary layers. Transfer of energy between wavenumbers plays a much less significant role in the dynamics of decay than in a non-rotating fluid. The decay rate of velocity fluctuations, both parallel and perpendicular to the rotation axis, remain closely coupled. Rotation produces a marked increase in the integral lengthscale parallel to the rotation axis. Hopfinger *et al.* (1982) studied the effect of rotation on a turbulent flow field produced by an oscillating grid in a rotating tank. Near the grid the turbulence is relatively unaffected by rotation. Farther from the grid, fluctuation amplitudes decrease, turbulent scales increase and, hence, rotation becomes important. Above the Ekman boundary layer, the flow field changes substantially, and remains independent of the depth thereafter. The flow there consists of concentrated vortices having axes parallel to the rotation axis, which extend throughout the depth of the container. Additionally, the vortex cores support waves (Maxworthy, Hopfinger & Redekopp 1985).

A flow where some of these ideas may be explored further experimentally is that of a fluid during impulsive spin-down to rest in a cylindrical container. Our attention is on the nature of the mean flow and the velocity fluctuations associated with it. Flow visualization and velocimetry are our tools in this experiment.

1.2. *Nature of spin-down to rest*

Consider a closed cylinder of diameter $2R$ and height H together with its fluid of kinematic viscosity ν, both rotating like a solid body at an initial angular velocity Ω_1. The Ekman number $E_i = \nu/\Omega_1 R^2$ is small (equivalently, the Reynolds number $Re_i = \Omega_1 R^2/\nu$ is large). At time $t = 0$, the container is abruptly stopped. During the next few radians of rotation of the core, thin axially symmetric Bödewadt boundary layers are established on the end disks (Bödewadt 1940). The thickness of these boundary layers is uniform and about $5[\nu/\Omega(t)]^{\frac{1}{2}}$, where $\Omega(t)$ is the slowly varying angular velocity in the core. The quasi-steady uniform ejection (Ekman pumping) over these disk boundary layers induces a slow axial flow and a corresponding radial outward motion in the core. The flow at the central plane of the cylinder looks much like that of an axially symmetric stagnation flow with swirl. The fluid, pushed out of the core at the central plane where the incoming axial streams collide, is returned to the Bödewadt boundary layers over the cylindrical wall. Hence, toroidal circulation cells are set up in the cavity.

The flow is unstable except at rather low Reynolds numbers. A critical Reynolds number $Re_{i,\,cr}$ for the flow during spin-down to rest in a cylinder can be estimated by

considering separately the respective critical values for the flows over the concave wall and the end disks. Neitzel (1982), using energy theory, suggest $Re_{i,cr} \approx 140$ as a lower bound for the stability of the flow over the cylindrical surface. Mathis & Neitzel (1985) determine experimentally the critical Reynolds number to be about $Re_{i,cr} \approx 350$ for the onset of the Taylor–Görtler vortices over the convave wall in a long cylinder ($H/2R = 9.35$). The critical Reynolds number for the flow over a stationary disk in rotating flow is about $Re_{i,cr} \approx 625$ (Savaş 1987). Therefore, the stability of the flow in the cylinder as a whole is determined by the stability of the flow over the concave wall. Hence, the overall flow should have a critical Reynolds number of $Re_{i,cr} = \Omega_i R^2/\nu \approx 350$ ($E_{i,cr} \approx 3 \times 10^{-3}$), set by the flow over the concave wall for aspect ratios of $H/2R$ of unity and higher. In steady rotation over an infinite disk, the boundary layer is turbulent (Savaş 1987). At sufficiently high Reynolds numbers, the flow over an end disk during impulsive spin-down to rest approximates that in steady rotation over an infinite disk, and is turbulent. The flow over the curved wall is characterized by the appearance of the Taylor–Görtler vortices within a few radians of revolution after the cylinder is stopped. These develop into a more complicated pattern and ultimately decay as spin-down is achieved (Greenspan 1968; Euteneuer 1972). These wall instabilities, the turbulent fluid convected through the Böewadt boundary layers, and the inertial waves transmitted within the rotating core give rise to flow velocity histories which appear to have the familiar characteristics of conventional turbulent flows. Our interest here is in the nature of these unsteady velocity histories in the cylinder, excluding the regions immediately over the concave wall and the end disks.

A working model of the flow which can predict the mean flow as well as the fluctuations during spin-down to rest in a cylinder is currently unavailable. The condition of axisymmetry imposed in their numerical experiments restricts Neitzel & Davis' (1981) results to the region over the concave wall in the cylindrical cavity. As an extension of Wedemeyer's (1964) model for the impulsive spin-up from rest, Weidman (1976*a*, *b*) has obtained the algebraic expression for the impulsive spin-down to rest:

$$\frac{\Omega(t)}{\Omega_i} = \frac{1}{(1+s)^2} \tag{1}$$

for the core flow, where s is the dimensionless time defined as

$$s = 0.69(2R/H)\,E_i^{\frac{1}{2}}\Omega_i t, \tag{2}$$

and the flow is assumed to remain laminar. The same result is also reported by Krymov & Manin (1986). We discuss below (1) as a model for the mean flow during spin-down to rest.

2. Experimental set-up and instrumentation

2.1. *Flow apparatus*

The rotating cylinder flow apparatus described in Savaş (1987) is used for velocity measurements in this experiment. The apparatus consists of a glass cylinder with an internal diameter $2R$ of 21.74 cm and height-to-diameter ratio $H/2R$ of 1.0 embedded in a 40 cm glass cubical aquarium (figure 1*a*). The working fluid is toluene (density $\rho = 0.87$ g/cm^3 and kinematic viscosity $\nu = 0.0067$ cm^2/s at 23 °C) and fills both the cylindrical cavity and that between the cylinder and the surrounding cube. The fluid

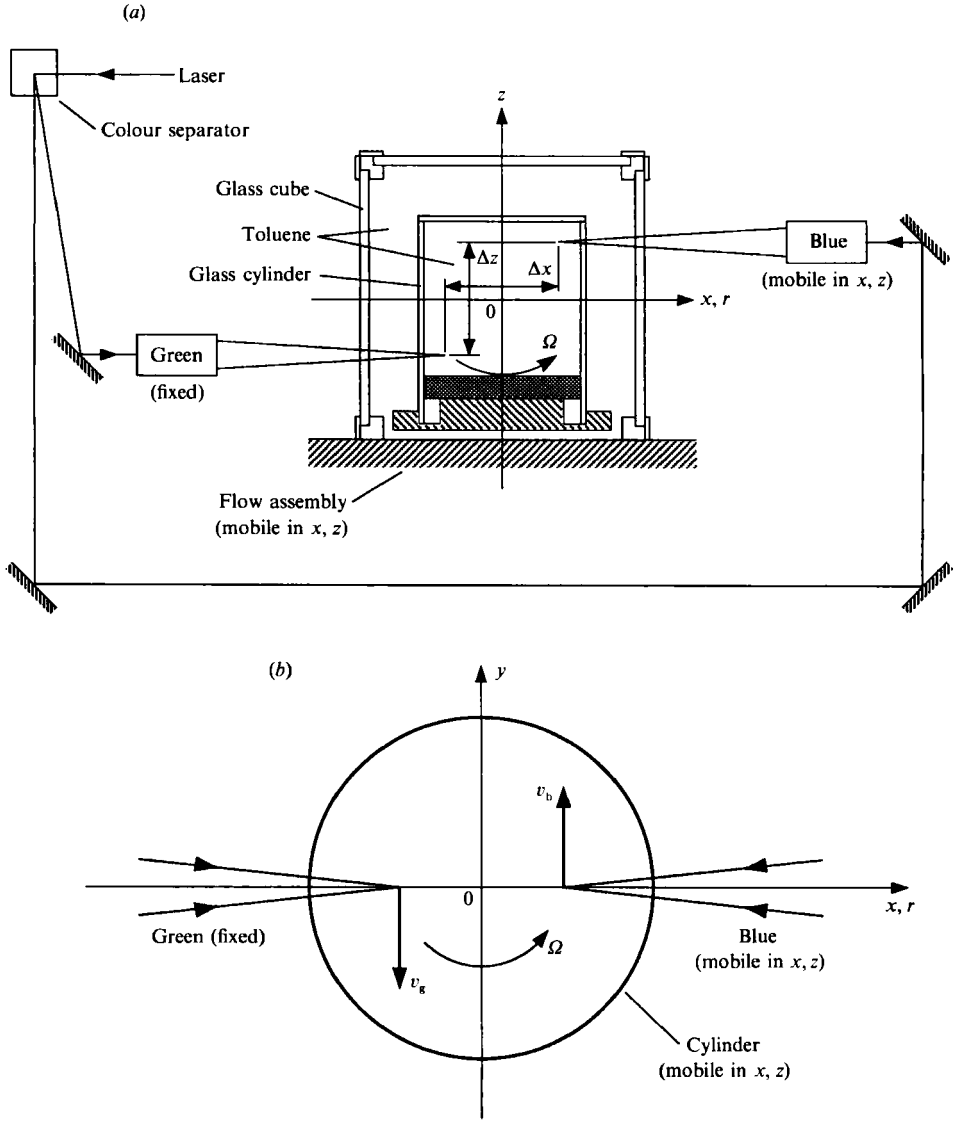

FIGURE 1(a,b). For caption see facing page.

inside the cylinder is seeded with 2 μm diameter uniform glass microspheres for laser-Doppler velocimetry. The particle number density is about 10^6 particles/cm^3. The index of refraction of toluene is 1.49 and that of the glass wall of the cylinder 1.47. This close match of the indices considerably reduces the aberration problem caused by the cylindrical surface during optical probing into the cavity. Additionally, the low kinematic viscosity of toluene makes low Ekman numbers $E_i = \nu/\Omega_i R^2$ possible at relatively low initial container speeds Ω_i. Flow visualizations are done in water in a lucite cylinder with a diameter of 21.3 cm and a diameter-to-height ratio of 1.0. The flow field is made visible by using reflective aluminium flakes in suspension (Savaş 1985). In the flow visualization experiments, the initial rotation speed Ω_i is increased to 9.77 rad/s to match the Ekman number $E_i = 9 \times 10^{-6}$ for the velocity measurements made in toluene at $\Omega_i = 2\pi$ rad/s. During flow visualization, the table

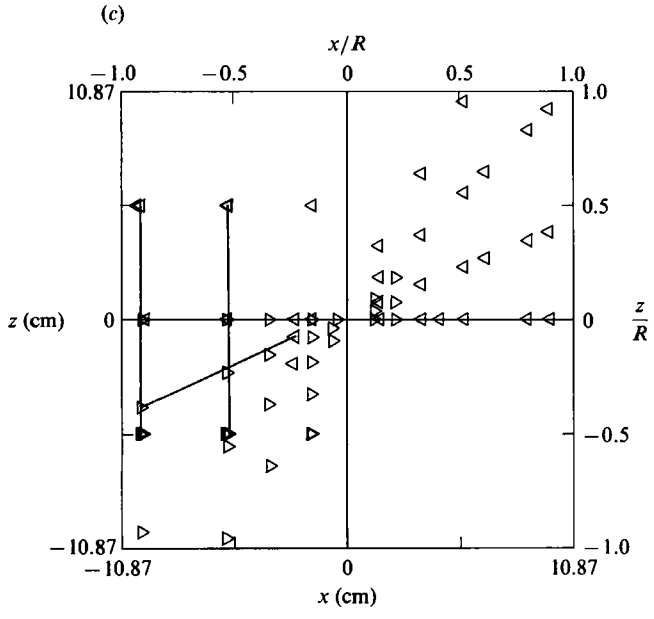

FIGURE 1. Experimental arrangements. (*a*) Overlay of the optical arrangement. Note that the blue probe and the cylinder assembly may be moved independently in the (r, z)-plane with respect to the green probe. Hence Δx and Δz may be independently set in the cylinder. (*b*) Plan view of the optical probes. The probes are in the (x, z)-plane. (*c*) Measurement domain: ▷, green probe and ◁, blue probe. Connected pairs correspond to the flows discussed in figures 8 and 9.

rotation and the camera triggers are coordinated by a computer. Of the sequences taken, here we present in figure 2 flows at dimensionless time $s = 0.5$ (cf. (1) and (2)). The deceleration of the turntable assembly is about 40 rad/s^2. The deceleration time of the cylinder is about two orders of magnitude smaller than the timescale of the flow $[0.69\,(2R/H)\,E_i^{\frac{1}{2}}\Omega_i]^{-1}$ predicted in (2), hence the spin-down process is impulsive in the experiments described here.

The centre of the cylindrical cavity is taken as the origin of the right-handed reference systems (figures 1*b* and 1*c*). Both Cartesian (x, y, z) and cylindrical (r, θ, z) coordinate systems are used. The z-axis in both coincides with the rotation axis of the cylinder. The x-axis is chosen in the direction of the propagation vector of the green beam. The radial coordinate r measures the distance from the rotation axis and the azimuthal coordinate θ measures the angle from the x-axis. The components of the velocity vector $\boldsymbol{u}$ in the respective coordinate systems are (u, v, w) and (u_r, u_θ, w). The separation of the two velocity probes is indicated by $(\Delta x, \Delta z)$ in figure 1 (*a*).

2.2. *Velocimetry*

The measurements are made with a two-component dual-beam laser-Doppler velocimeter (LDV) shown in figure 1 (*a*). The green and the blue light beams from an argon ion laser (with respective wavelengths of 514.5 and 488.0 nm) are used for probing the flow. The transmitting optics assembly for the green beam is fixed and that for the blue beam is mounted on a two-dimensional traverse system as sketched in figure 1 (*a*). This arrangement enables the blue optics to move along the z- and x-axes. Thus, the green and the blue probes can be positioned arbitrarily relative to each other in the (x, y)-plane. The two probes can be positioned at the same point in the cylinder. This combination of the probes and the three-dimensional traverse

(a)

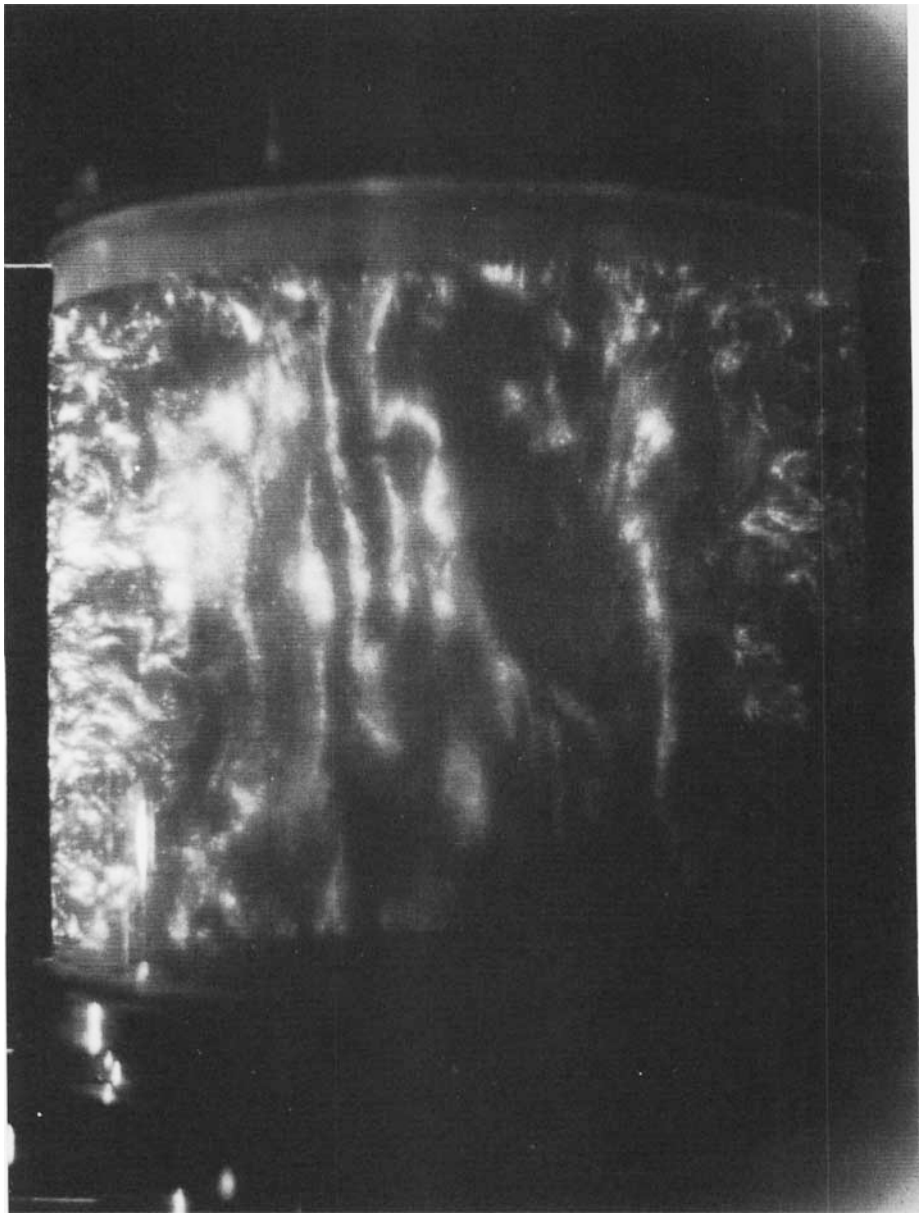

FIGURE 2(a). For caption see page 537.

mechanism on which the rotating flow apparatus is mounted makes spatial velocity correlation calculations possible. Signals are collected from the probe volumes at about 10° to the incident beams and focused on the photomultiplier tubes of the receiving optics assemblies. All velocity measurements are made in the (x, y)-plane ($y = 0$ plane). In this study only the azimuthal velocity component v (or equivalently, u_θ) is measured (figure 1*b*).

Signal conditioning and counting are done using Thermal System Inc. TSI-1990 hardware. Data acquisition and processing are done by a computer. The free running

(*b*)

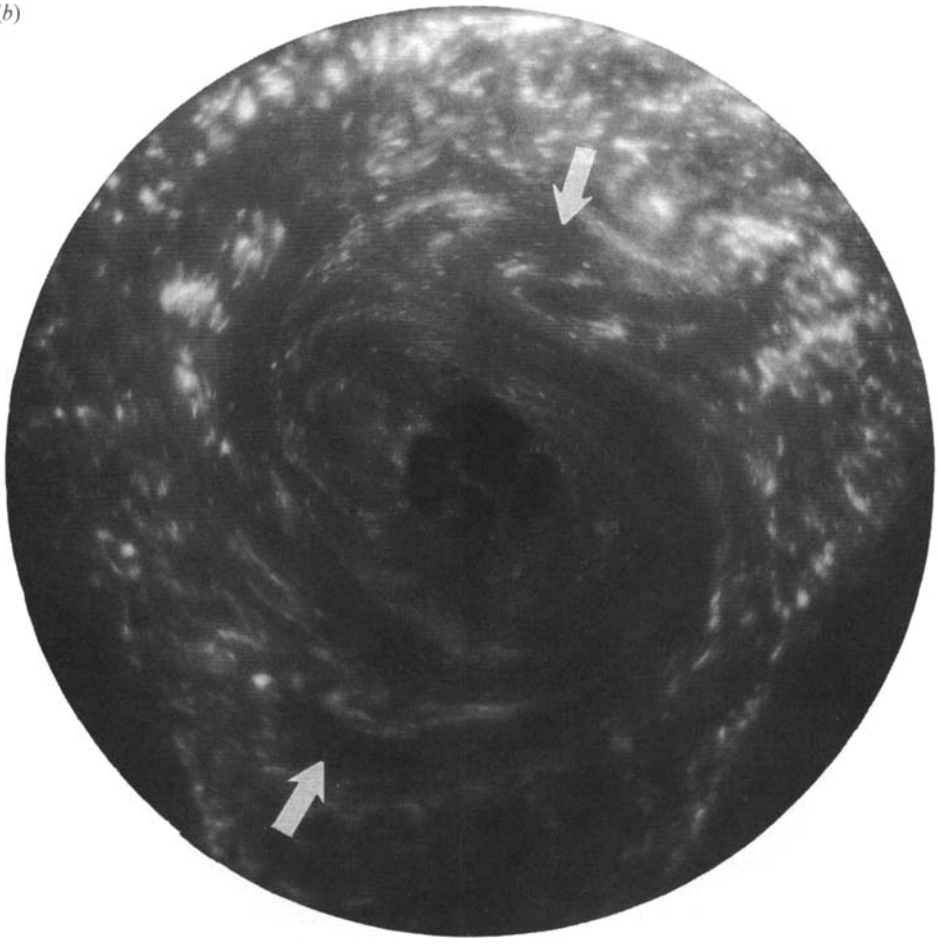

FIGURE 2(*b*). For caption see page 537.

data rates of the two counters are at least an order of magnitude higher than the sampling rate. The sampling rate is controlled by a preset counter. Sampling cycles are initiated by the counter and the elapsed times between successive samples are recorded independently by the hardware for construction of velocity time histories. A typical experiment starts after the cylinder assembly has been rotating at a constant speed for about 30 min. Numerous preliminary runs indicated the necessity of such a long spin-up time to allow the inertial oscillations to subside and the contents of the cylinder to reach solid-body rotation. Once steady state is reached, the data acquisition sequence is started. The time $t = 0$ mark from the servo amplifier starts the actual data acquisition. A transient data record lasts 1 to 3 min.

3. Flows

3.1. *Scope of experiments*

The subject matter is the nature of the flow in the core during impulsive spin-down to rest. Most of the measurements are carried out in the interior of the fluid covering a radial range of $r/R \leqslant 0.9$ and the vertical range of $-0.48 < z/H < 0.48$. No

(*c*)

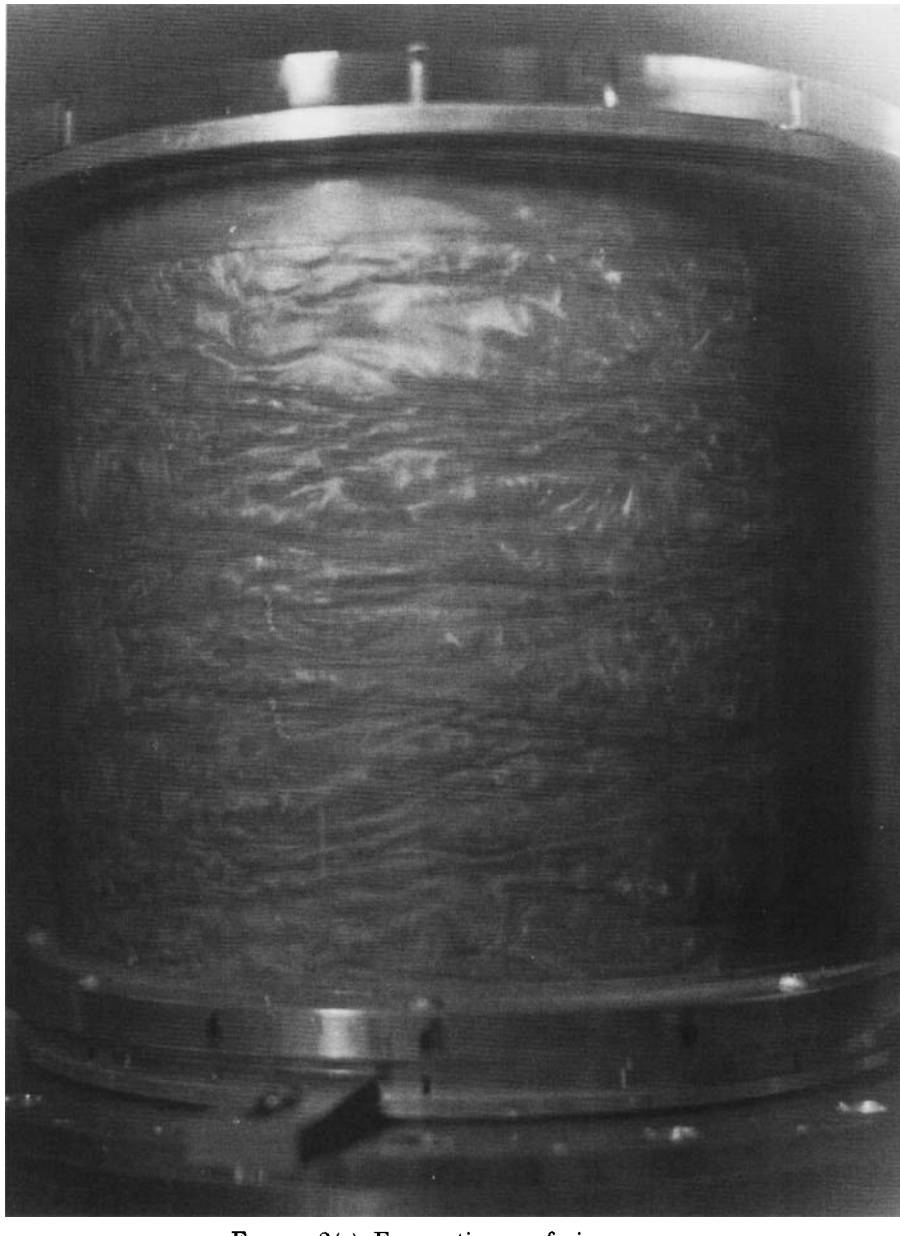

FIGURE 2(*c*). For caption see facing page.

detailed measurements are made over the curved wall where Taylor–Görtler vortices are likely to be dominant. An experimental study of the boundary layers over the disks may be found in Savaş (1987). Measurements are presented for two nominal initial angular velocities of $\Omega_i = \pi$ rad/s ($E_i = 1.8 \times 10^{-5}$) and $\Omega_i = 2\pi$ rad/s ($E_i = 9 \times 10^{-6}$) of the cylinder. Velocity data are taken along seven lines (rays) in the (x, z)-plane (alternatively, (r, z)-plane). These lines or rays are at angles of 0° ($\Delta x =$ 7.4 cm, $\Delta z = 0$), 24.2° ($\Delta x = 7.4$ cm, $\Delta z = 3.3$ cm), 47.5° ($\Delta x = 7.4$ cm, $\Delta z = 8.0$ cm), 62.2° ($\Delta x = 7.4$ cm, $\Delta z = 13.9$ cm), and 90° ($\Delta x = 0$, $\Delta z = 5.4$ and 10.8 cm) with

(*d*)

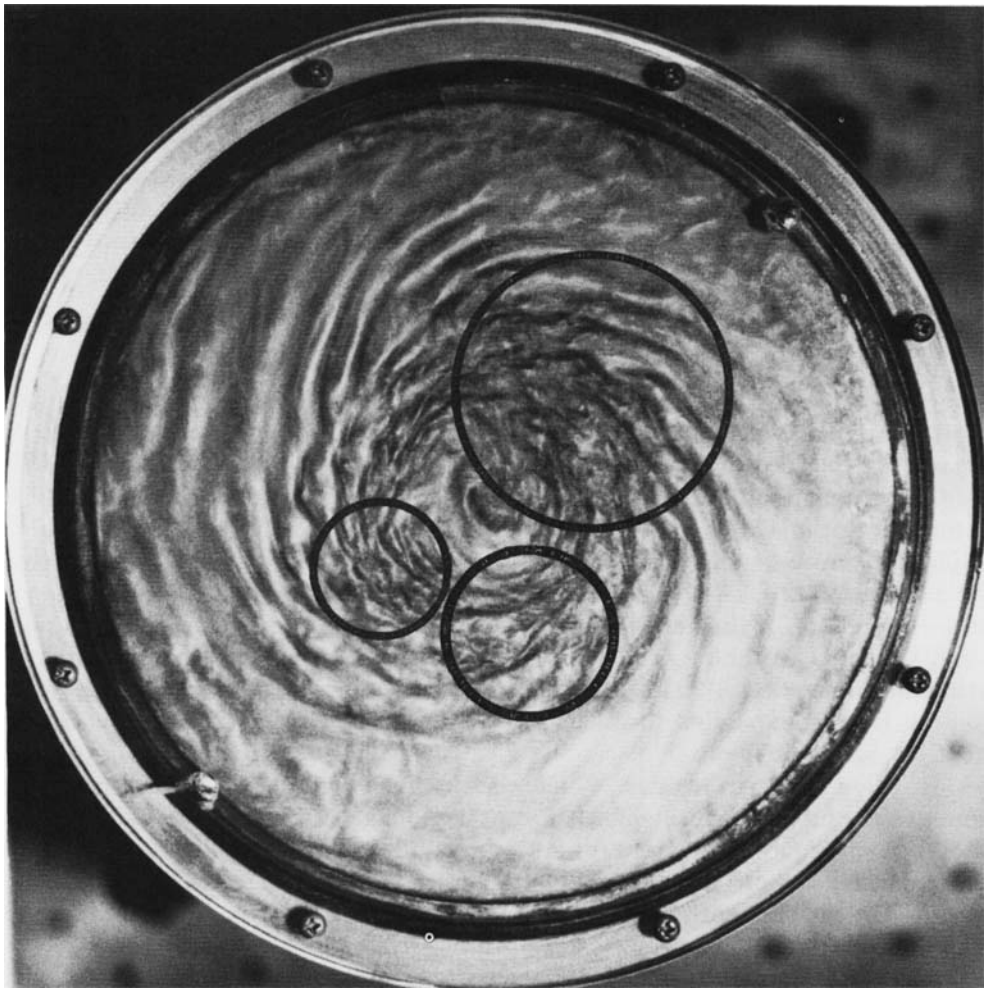

FIGURE 2. Flow visualization during spin-down to rest. Photographs are taken in a 21.3 cm diameter lucite cylinder with a diameter-to-height ratio $2R/H$ of 1. Flow field is made visible using reflective aluminium flakes in water. The initial rotation rate Ω_i is increased to 9.77 rad/s to match the Ekman number $E_i = \nu/\Omega_i R^2$ of 9×10^{-6} for the velocity measurements made in toluene at $\Omega_i = 2\pi$ rad/s. All pictures are taken at $t = 25$ s ($s = 0.5$). (*a*) Taylor–Proudman columns in meridional cross-section. Sheet of laser light is illuminating from the right and passing through the cylinder axis. Note that the light intensity is attenuated due to the flake suspension and the radial distance is distorted due to the lens effect of the cylinder. (*b*) Taylor–Proudman columns in diametral cross-section. Sheet of laser light is at the midplane of the cylinder and perpendicular to the axis. Note that the focusing of the light sheet partially compensates for its attenuation in the flake suspension, at the expense of observable field of view. The arrows point to large axially aligned vortices. (*c*) Taylor–Görtler vortices over the concave wall under diffuse illumination in dense flake suspension. The visible depth is about 3 mm. (*d*) End view over the disk under diffuse illumination in dense flake suspension. The visible depth is about 3 mm. The circled regions are thought to be the footprints of vortices similar to those marked in figure 2(*b*).

respect to the horizontal axis (figure 1*a*, *c*). The intended angles were 0, $\frac{1}{8}\pi$ (22.5°), $\frac{1}{4}\pi$ (45°), $\frac{1}{3}\pi$ (60°), and $\frac{1}{2}\pi$ (90°) radians. The slip is due to a computer programming error. The locations of the green and blue probes are arranged such that the measurement points (probe volumes) are approximately on the desired ray. Measurements are

made at seven configurations on each of the 0°, 24.2°, and 47.5° rays and at three configurations on the 62.2° ray. In addition, further measurements are done on each of the three vertical lines (parallel to the rotation axis) at radial locations r/R of 0.16, 0.53, and 0.91 (figure 1*c*). For each configuration, experiments are repeated usually three times for each initial rotation speed. One set of data is recorded at constant speed (π rad/s) at each probe configuration to verify the probe location through velocity measurements in solid-body rotation. The data sampling rate is 5 Hz for $\Omega_i = \pi$ rad/s and 10 Hz for $\Omega_i = 2\pi$ rad/s. The free-running data rates of the counters are at least an order of magnitude higher than the sampling rates used during measurements. The measurements on the three vertical rays are repeated at a 20 Hz sampling rate for $\Omega_i = \pi$ rad/s and 40 Hz for $\Omega_i = 2\pi$ rad/s.

3.2. *Flow visualization*

Figure 2 shows some flow visualization pictures taken in the lucite cylinder during spin-down to rest. The flow field is made visible by using reflective aluminium flakes in water. All pictures are taken at the initial Ekman number of $E_i = \nu/\Omega_i R^2 = 9 \times 10^{-6}$ corresponding to the flow in the toluene filled glass cylinder at $\Omega_i = 2\pi$ rad/s. The initial rotation rate Ω_i is increased to 9.77 rad/s to match the Ekman number. The pictures are taken at $t = 25$ s which corresponds to the dimensionless time of $s = 0.5$ (equation (2)). The photograph in figure 2(*a*) is a meridional cross-section and that in figure 2(*b*) a diametral one. The aluminium-flake number density is low enough to allow the illumination of the entire cross-section, yet high enough for continuous light reflection off the flakes. In these two pictures, the light beam of the argon-ion laser is expanded to a sheet of about 1.5 mm thick for illumination. In figure 2(*a*), about 90% of the meridional plane is visible, and in figure 2(*b*), the laser sheet is being focused in the cylinder. The flake suspension, however dilute, attenuates the intensity of the light sheet as it propagates through the cylinder. The photographs in figures 2(*c*) and 2(*d*) are taken under diffuse illumination. The flake number density is more than an order of magnitude higher than that in figures 2(*a*) and 2(*b*). The visible depth is about 3 mm in both pictures. They essentially reveal the flow in the immediate vicinity of the transparent walls.

The picture in figure 2(*a*) shows that the flow in the core is fundamentally different than that at the perimeter. The long bands of light strips extend almost from disk to disk maintaining their alignment with the axis, barring some undulations. The cross-sectional view in figure 2(*b*) verifies the different nature of the flows in the core and at the perimeter. The flow in the core consists of large vortices aligned with the rotation axis of the cylinder. The flakes align themselves along the stream surfaces when subjected to sufficient shear. Since the flow in the core is mostly aligned with the cylinder axis, the flakes tend to align with their normal perpendicular to the rotation axis and, therefore, to the observation direction in figure 2(*b*). Consequently, the visualization is inherently poor and the core region looks darker. Even within this faint light field, the signatures of the vortices seen in figure 2(*a*) are identifiable in figure 2(*b*), where two large vortices are marked with white arrows. The flow at the perimeter is reminiscent of developed three-dimensional turbulence.

Figure 2(*c*) shows the signature of the flow over the concave wall of the cylinder. The flow consists mostly of azimuthal turbulent vortices. Their lateral spacing continually increases as the flow matures. The evolution of these Taylor–Görtler vortices is studied in detail by Euteneuer (1972), Neitzel & Davis (1981), and Mathis & Neitzel (1985). The pictures in figure 2(*a–c*) suggest that the flow has two substantially different regions: the core which consists of vortices aligned with the

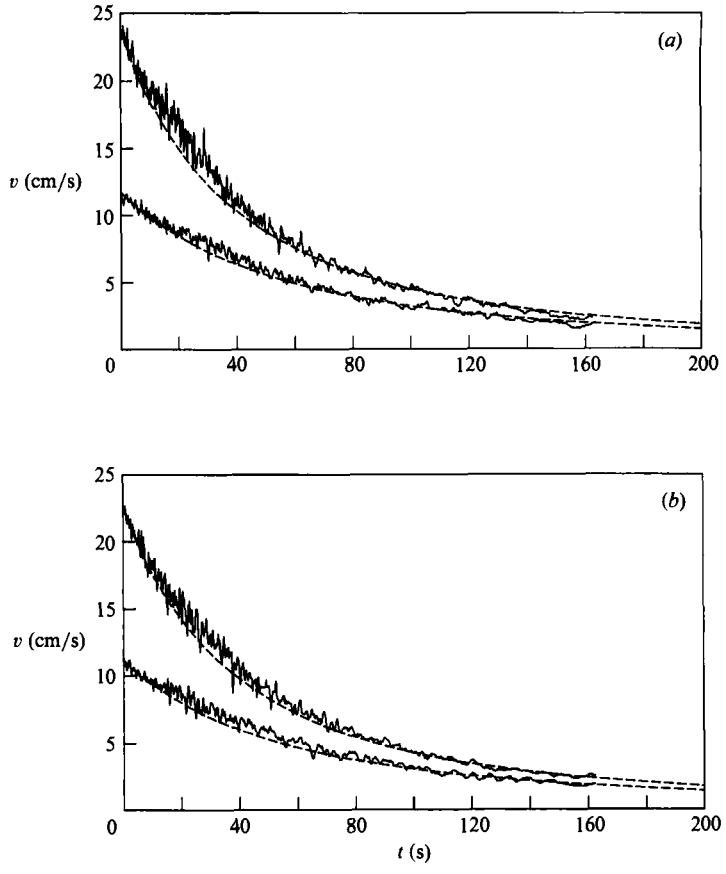

FIGURE 3. Measured transient velocity signals (solid lines) and theoretical mean flows (dashed lines, from equation (1)) during spin-down to rest; upper traces for $\Omega_1 = 2\pi$ rad/s and lower traces for $\Omega_1 = \pi$ rad/s. (*a*) Green probe at $(x, z) = (-3.76$ cm, 0) and (*b*) blue probe at $(x, z) = (3.57$ cm, 0).

rotation axis, and the perimeter which consists of azimuthal vortices enveloping the core. The structures in the core resemble Taylor–Proudman columns and those at the perimeter are akin to Taylor–Görtler vortices.

The signature of the flow on the disk is shown in figure 2(*d*). The picture shows mostly Type II waves (Class A) with patches of intense turbulence. The footprints of vortices similar to those marked in figure 2(*b*) are not readily identifiable on the figure. However, we speculate that the circled regions are the footprints of axial vortices. We base our speculation on the notion that the axial vortices create locally finer scale turbulence because of their lower intrinsic Ekman numbers (equivalently, higher Reynolds numbers) due to the locally higher angular velocities at their cores. Note that the photographs in figures 2(*b*) and 2(*d*) are not simultaneous owing to the nature of the visualization technique used here. We return below to the question of signature on the disk in connection with the formation of a single vortex during the final phase of the flow.

3.3. *Flows*

Figure 3 shows sample velocity measurements at $\Omega_1 = \pi$ and 2π rad/s. The traces are simultaneous in pairs of green and blue. The unsteady velocity traces $v(t)$ (equivalently, $u_\theta(t)$) illustrate the turbulent nature of the spin-down process at the

low Ekman numbers of the experiment. The predictions of (1) are shown as the dashed lines over the traces in the figure. Evidently, that prediction is successful if all that is needed is a timescale of the transient mean flow. That the prediction does not follow the measurements more closely is expected. The assumption behind (1) is that the end disks eject the fluid into the core at the rate determined from the solution of the laminar Bödewadt flow. The critical Reynolds number of that laminar flow is rather low and the boundary layer is almost always turbulent in a flow simulating rotating flow over a stationary disk. The turbulent boundary-layer profile over the disk, however, shows a close resemblance to its laminar counterpart (Savaş 1987). Perhaps this resemblance of the profiles is the reason for the success of (1) in predicting the spin-down timescale.

Our interest here is in the velocity fluctuations. Clearly, we cannot take the difference between the measurements and the prediction of (1) to determine the fluctuations. The remainder of this paper discusses a method of extracting the fluctuations and their subsequent interpretation.

4. Discussion

4.1. *Mean flow*

A common feature of all the measurements is the onset of strong fluctuations, the amplitudes and frequencies of which decay progressively as the flow decelerates. The information hidden in those fluctuations is the major concern of this article. An acceptable scheme must be devised to extract the fluctuation velocities from the few transient velocity histories. The rigorous method is to ensemble-average traces like those shown in figure 3 over sufficiently many realizations. In order to get a meaningful ensemble average, one needs on the order of hundreds of repetitions of the experiment under identical conditions. As stated in §2.2 above, each realization requires about 30 min, and such an undertaking is excessively time consuming. The scheme used here is to identify a *mean* flow for each realization and obtain the fluctuations by taking the difference between this mean and the measured trace. An immediate candidate for the mean flow is the analytical prediction in (1). Clearly, that is not an acceptable model of the mean flow for this purpose as may be seen in figure 3. We choose to fit curves to the data to describe their mean behaviour. A spectral curve fitting technique is used here. The essence of the scheme is clear from the traces in figure 3. *The timescale of the fluctuations is much smaller than that of the transient bulk flow.* Therefore, a suitably chosen low-pass filter should produce an adequate fit to describe the mean flow. The velocity histories are reconstructed at 1024 samples per trace for spectral analysis. Further, the traces are arranged to obtain a 4096-sample long periodic signal. An original velocity trace like those shown in figure 3 is now the first quarter of a periodic signal that looks like, say, a negative sinuous curve (figure 4*a*). Then, this pseudosignal is Fourier transformed into frequency domain via an FFT program. A low-pass Gaussian filter is used to isolate the mean flow $\langle v(t)\rangle$. The fitted smooth curve obtained from this calculation along with the prediction of (1) are shown in figure 4(*b*). The spectrally fitted curve describes the mean flow adequately. The result is insensitive to the width of the filter as the respective spectral components of the mean flow and the fluctuations are well separated in the frequency domain. We now take the difference between the instantaneous velocity $v(t)$ and the mean velocity $\langle v(t)\rangle$ as the fluctuating velocity component $v'(t)$, that is

$$v(t) = \langle v(t)\rangle + v'(t). \tag{3}$$

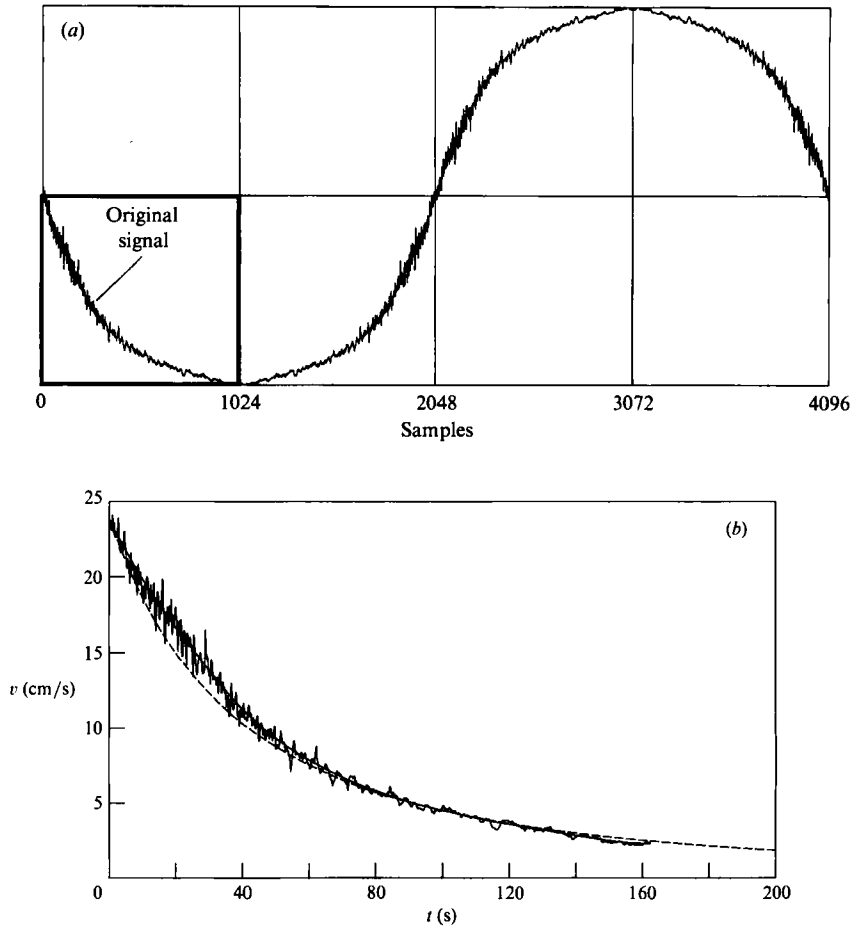

FIGURE 4. Spectral curve fitting to extract fluctuations. The upper trace in figure 3(*a*) is used for illustration. (*a*) Periodic signal construction for FFT. Reflections of the original trace are concatenated to construct a quasi-periodic mean flow suitable for FFT processing. (*b*) Raw signal, theoretical model for the mean flow (dashed line), and the spectrally fitted mean flow (solid smooth line).

The fluctuation histories $v'(t)$ obtained from the traces in figure 3 are shown in figure 5. The fluctuation amplitudes and frequencies are decreasing as the flows slow down. We propose below a scaling which should elucidate the nature of these fluctuations.

4.2. *Scaling*

Intense velocity fluctuations exist during the spin-down process as exemplified in figures 3 and 5. The amplitudes and frequencies of these fluctuations decrease as the flow decelerates. If the fluctuating velocity component $v'(t)$ is scaled with the slowly decaying local mean velocity $\langle v(t)\rangle$ as

$$\tilde{v}(t) = v'(t)/\langle v(t)\rangle \tag{4}$$

to underscore its relative amplitude, we find that the fluctuations are equally dominant during the whole spin-down process. However, the frequencies of these oscillations decrease as the flow slows down (figure 5). According to Taylor's

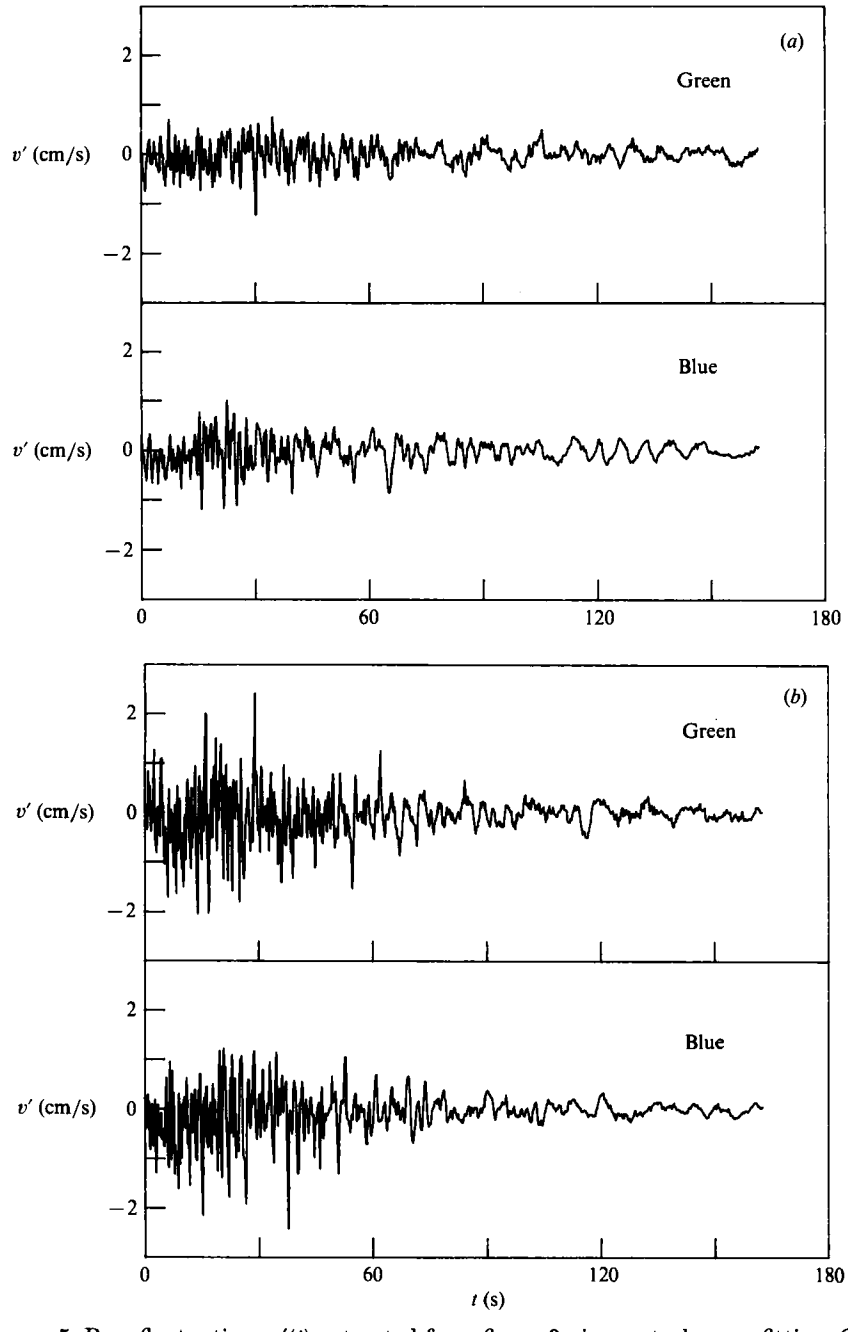

FIGURE 5. Raw fluctuations $v'(t)$ extracted from figure 3 via spectral curve fitting. Green probe at $(x, z) = (-3.76$ cm, 0) and blue probe at $(x, z) = (3.57$ cm, 0). The traces correspond to those in figure 3. (*a*) $\Omega_i = \pi$ and (*b*) $\Omega_i = 2\pi$ rad/s.

hypothesis, for fixed-size eddies high frequencies are recorded by a stationary probe when the mean velocity is high and low frequencies when the mean velocity is low. During the spin-down process, observed frequencies therefore decrease if eddies of a persistent size are presumed present. To elucidate the use of this assumption, the time axes of the velocity fluctuations in figure 5 are rescaled using the spectrally

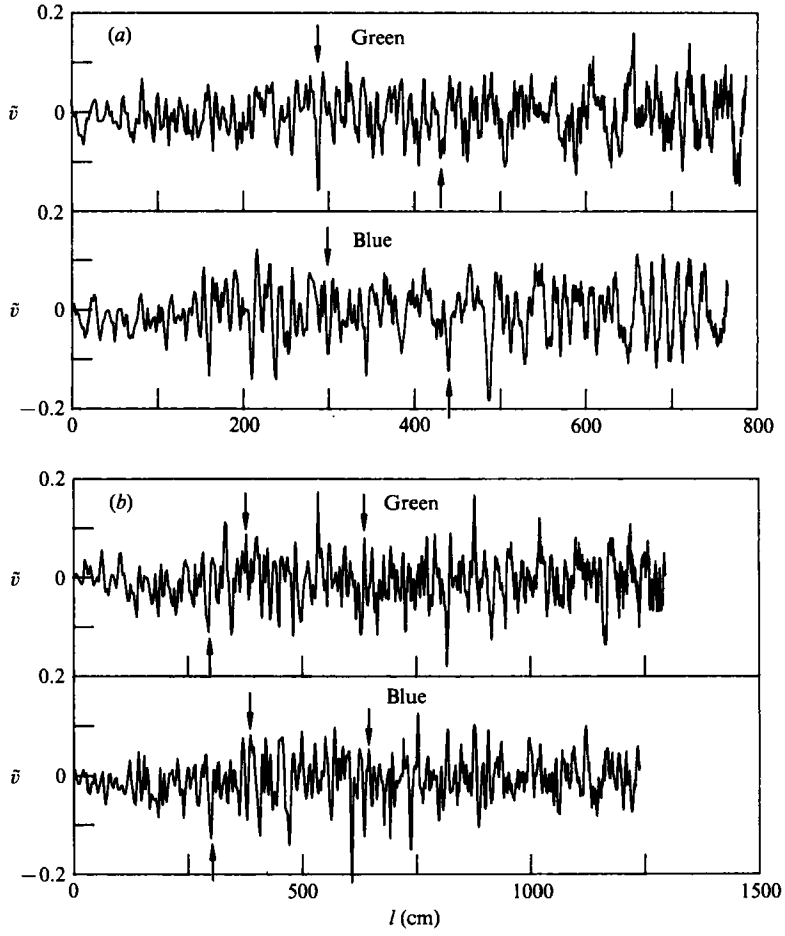

FIGURE 6. Rescaled velocity fluctuations $\tilde{v}(l)$ during spin-down to rest as function of distance travelled $l = \int_0^t \langle v(t) \rangle \, \mathrm{d}t$. Green probe at $(x, z) = (-3.76 \text{ cm}, 0)$ and blue probe at $(x, z) = (3.57 \text{ cm}, 0)$. The traces correspond to those in figure 5. Pairs of arrows indicate signatures lagging each other by about πr (half a revolution). (*a*) $\Omega_1 = \pi$ and (*b*) $\Omega_1 = 2\pi$ rad/s.

fitted mean flows $\langle v(t) \rangle$, such as that shown in figure 4(*b*). With the use of this new scaling

$$\mathrm{d}\tau = \langle \Omega(t) \rangle \, \mathrm{d}t \tag{5a}$$

or, equivalently,

$$\mathrm{d}l = \langle v(t) \rangle \, \mathrm{d}t \tag{5b}$$

the initial regions of the raw traces in figure 5 are expanded and the final phases contracted. Note that $\langle v(t) \rangle = \langle \Omega(t) \rangle r$, hence, $l = r\tau$ at a given measurement location, where τ is the arc traversed by the fluid and l the distance travelled. The results are shown in figure 6. The time axes in the figure are now the linear scales of the distance travelled by the mean flow at the probe location in the cylinder. Comparable spatial frequencies with comparable amplitudes are persistent in the flow. Presumably, that behaviour should persist indefinitely if the fluid domain were unbounded. Most of the ensuing discussions are based on the analysis, in particular on the spectral analysis, of the rescaled data. The fluctuation data are first rescaled as described in (4) and (5) (cf. figures 4, 5 and 6), and subsequently resampled into 1024 equispaced intervals using linear interpolation, now as a function of the

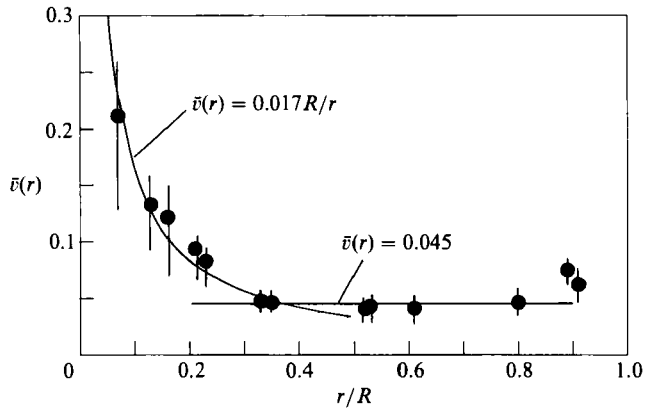

FIGURE 7. Normalized root-mean-squared fluctuation intensity $\bar{v}(r)$ in the cylinder during impulsive spin-down to rest. The data are normalized both for the amplitude and the time. The weighted averages are shown as circles. Measurements for $x < 0$ and $x > 0$ appear as closely spaced pairs. The line $\bar{v}(r) = 0.017R/r$ is a curve fit to data in the core region ($r/R < 0.4$) and $\bar{v}(r) = 0.045$ is the suggested uniform value in the buffer region ($0.4 < r/R < 0.8$).

distance travelled l. All correlations and spectral estimations are calculated using FFT routines. Power spectral estimations are obtained using overlapping segments of data records like those shown in figure 6. The segments are passed through the *Welch window* for acceptable leakage in power spectral density (see, for example, Press *et al.* 1986).

4.3. *Fluctuation intensities*

Having invoked Taylor's transformation, we now examine the fluctuation intensities so scaled. The dimensionless time τ is now defined as $\mathrm{d}\tau = \langle \Omega(t) \rangle \, \mathrm{d}t$ and, equivalently, the distance l as $\mathrm{d}l = r\langle \Omega(t) \rangle \, \mathrm{d}t$. We define the dimensionless root-mean-squared (r.m.s.) fluctuation intensity $\bar{v}$ as

$$\bar{v}^2 = \frac{1}{T} \int_0^T \tilde{v}(\tau)^2 \, \mathrm{d}\tau \tag{6a}$$

or, equivalently, as

$$\bar{v}^2 = \frac{1}{L} \int_0^L \tilde{v}(l)^2 \, \mathrm{d}l, \tag{6b}$$

where $T = \int \mathrm{d}\tau$ and $L = \int \mathrm{d}l$ are the scaled record lengths (cf. (5)). The values for $\bar{v}$ are calculated from data such as those shown in figure 6 and are plotted in figure 7 as a function of the radial position in the cylinder. The figure contains results from all realizations at $\Omega_\mathrm{i} = \pi$ and 2π rad/s except the few measurements very close to the ends of the cylinder (cf. figure 1*c*). The symbols in the figure are the weighted averages and the vertical bars show the range of scatter in individual measurements. The scatter in the data is not systematic, that is, the scatter does not show any identifiable dependence on the initial rotation rate Ω_i or on the axial position z. *Variations among realizations under identical conditions as well as between flows starting at* $\Omega_\mathrm{i} = \pi$ *and* 2π rad/s *are not significant. Our premise in using single transient experiments to infer the general statistics of the flow is the ergodicity of the scaled flows.* The data in figure 7 support this assumption *a posteriori*.

Even though the mean and fluctuation velocities at the centre become vanishingly small, the scaled fluctuations there are most dominant. A curve fit to the data in figure 7 suggests $\bar{v} \approx 0.017(R/r)$ dependence over the range $r/R \leqslant 0.4$ at the *core*.

Since the flow structures in the core are aligned with the rotation axis (cf. figure 2*a*), the azimuthal velocity measurements capture the most active component of the velocity vector there. The fluctuation intensity is more or less uniform over the range $0.4 < r/R < 0.8$, which acts as a *buffer* region between the core and the flow over the concave wall. The value of $\bar{v} \approx 0.045$ is a suggested constant value for the turbulence intensity in this buffer region. The flow over the cylindrical wall is predominantly azimuthal and the major axes of the LDV probe volumes are aligned with the mean gradient of the azimuthal velocity component, therefore the turbulence intensity measurements there suffer from poor spatial resolution. It is clear, however, that the flow maintains a uniform turbulence intensity during its adjustment from the axially aligned core to the azimuthally dominant perimeter. Correlations and spectral calculations below corroborate these results.

4.4. *Correlations*

The rescaled fluctuation traces $\tilde{v}$ in figure 6 are qualitatively similar not only between the simultaneous pairs but also between traces for $\Omega_i = \pi$ and 2π rad/s. This lends further support to our underlying assertion of the ergodicity of the flow. One can visually identify signatures that are slightly lagging each other on the simultaneous velocity pairs as marked in the figure. One can even estimate that lag to be about πr (half a revolution). Since the probes are located diametrically opposite each other, one concludes that the flow in the core consists of slowly varying structures that register comparable signatures at the probes as they move through the measurement locations. That provides support for our use of Taylor's frozen eddy hypothesis in the scaling of (5). Auto- and cross-correlations of $\tilde{v}$-traces are calculated to elucidate the structure of the flow within the cylinder and some sample correlation plots are shown in figure 8(*a–c*). Each frame in the figure contains the two autocorrelations corresponding to the green and blue probes, and their cross-correlation is shown in figures 8(*a*) and 8(*b*). Figure 8(*a*) shows a sample in the vicinity of the cylindrical wall where the flow has a predominantly azimuthal structure. The two probes are on a line parallel to the axis of rotation and are at $r/R = 0.91$ and $0.5H$ apart. Their autocorrelations and cross-correlation are poor. The probes are essentially recording independent flow features. Figure 8(*b*) shows clearly the Taylor–Proudman columns in the core of the cylinder and is as a quantification of the vertical structure pictured in figures 2(*a*) and 2*b*). The two probes are in line at $r/R = 0.54$ and $0.5H$ apart in the z-direction. The persistent similarity between the two traces, which are recorded so far apart, indicates that the vortices present extend over large axial distances, probably from one end of the cylinder to the other. This result is independently arrived at by Hopfinger *et al.* (1982) in their study of turbulence in a water tank. Figure 8(*c*) shows the autocorrelations of the velocity traces in the core ($x_b/R = -0.23$) and over the curved wall ($x_g/R = -0.91$). The autocorrelation curve for the blue probe located in the core shows sinuous oscillations which are indications of the stable vertical vortical structures photographed in figures 2(*a*) and 2(*b*). The autocorrelation of the green probe does not show any behaviour comparable to the blue one. The poor correlation essentially establishes the independence of the core flow from that over the concave wall.

4.5. *Power spectra*

Autopower spectra corresponding to the samples in figure 8 of the scaled data $\tilde{v}$ are shown in figure 9. The figure shows relative amplitudes in arbitrary units as a function of the wavenumber k for various regions of the flow. The wavenumber is

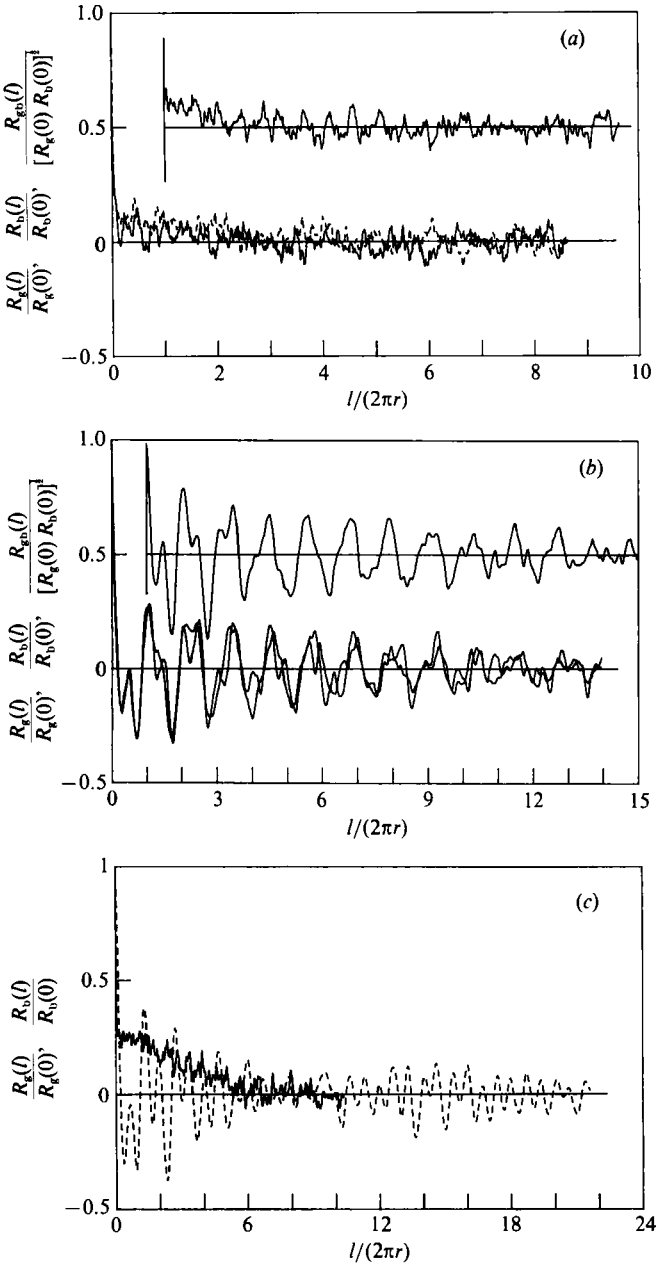

FIGURE 8. Autocorrelations R_g and R_b of the normalized data from the green (——) and blue (– – – –) probes in various regions of the cylinder. Their cross-correlations R_{gb} are also shown in (*a*) and (*b*) as traces displaced one tic mark along both axes. See figure 1 (*c*) for the corresponding probe locations. (*a*) Poorly correlated signals in the vicinity of the cylindrical wall. No discernible feature is identifiable in either the autocorrelations or the cross-correlation. The blue probe is at $(x/R, y/R, z/H) = (-0.91, 0, +0.25)$ and the green probe at $(x/R, y/R, z/H) = (-0.91, 0, -0.25)$. (*b*) Well-correlated signals from axially separated probes in the core, an indication of the axially coherent Taylor–Proudman columns. Simultaneous velocity traces from probes on a line parallel to the axis of the cylinder. The blue probe is at $(x/R, y/R, z/H) = (-0.53, 0, +0.25)$ and the green probe at $(x/R, y/R, z/H) = (-0.54, 0, -0.25)$. (*c*) Poorly correlated signals from near the curved surface and the core of the cylinder. The green probe is over the cylindrical wall at $(x/R, y/R, z/H) = (-0.91, 0, -0.38)$ and the blue probe in the vicinity of the centre at $(x/R, y/R, z/H) = (-0.23, 0, -0.08)$. The sinuous oscillations are on the autocorrelation curve for the blue probe which is located in the core.

non-dimensionalized locally as $2\pi rk$, hence, $2\pi rk = 1\,[\log(2\pi rk) = 0]$ corresponds to one wave per revolution at the probe location. That the flow visualization pictures in figure 2 show distinct regions in the cylinder, that the scaled fluctuation intensities in figure 7 in various regions of the flow show varying mean amplitudes, and that the correlations in figure 8 exhibit well-correlated flow regions in the core but poorly correlated regions over the concave wall suggest that the corresponding power spectra should exhibit distinguishable behaviour in various regions. The autopower spectra curves in figure 9(*a*) correspond to the flow over the concave wall, the correlations of which are shown in figure 8(*a*). The power spectra show a slow dependence on the wavenumber k. The power spectra of the flow in the core, shown in figure 9(*b*), however, is clearly different than those at the perimeter. The fluctuation amplitudes show a faster decay rate with the wavenumber k. The corresponding correlation plots in figure 8(*b*) show strong axial correlation in the core. The double peak in the spectra, observable in this particular sample and also evident in the correlation plot in figure 8(*b*), corresponds to pairing of vortices during the evolution of the flow towards a single concentrated vortex, as discussed below. Figure 9(*c*) shows autospectra for the flow in the core and at the perimeter and corresponds to the conditions in figure 8(*c*). The blue probe is in the core ($x_b/R = -0.23$) and the green probe near the cylindrical wall ($x_g/R = -0.91$). The spectrum of the velocity trace recorded by the blue probe shows a faster decay rate with k while the simultaneous trace recorded by the green probe exhibits a slower decay. Figure 10 shows the estimated k^{-n} dependency of the power spectra of the scaled velocity fluctuations in the cylinder. The exponent n is determined from a least-squares curve fit to spectral curves like those shown in figure 9 for $2\pi rk > 2$. The vertical bars in the figure indicate the extreme values. The scatter reflects the dependence on the axial position. The average value for 418 flows used to construct the figures is about 2.6 ∓ 0.7. The amplitude of power spectra decreases more rapidly with the wavenumber in turbulence in the cylinder than the homogeneous turbulence.

4.6. *Concentrated vortex*

An obvious question brought up by the scaling used to arrive at figure 6 from figure 5 (equation (4)) is the nature of the eventual decay of the flow. During the decay, as the eddy size increases, its growth will no longer be unrestricted when its size becomes comparable to that of the cylinder. We observe that the last phase of the flow tends to a single vortex in the core, not necessarily coaxial with the cylinder. The evidence for this behaviour is present in both the flow visualization experiments and the velocity measurements. An example may be seen on the lowest trace in figure 3(*b*), or equivalently in its rescaled forms, on the lowest traces in figures 5 and 6. The quasi-periodic signal seen after about 120 s on the last trace in figure 3(*b*) is evidently the signature of a precessing vortex. That signature is most clearly identifiable on the corresponding rescaled trace in figure 6(*a*).

Figure 11 shows instantaneous angular velocity profiles $\langle\Omega(r/R, s)\rangle/\Omega_i$ in the cylinder at selected times $s = 0.69(2R/H)\,E_i^{\frac{1}{2}}\Omega_i t$. The data points in the figure are averages over one-revolution segments of the velocity histories starting at dimensionless times $s = 0.10$, 0.25, 0.50, 1.9, and 1.8. The figure is constructed from all measurements for $\Omega_i = \pi$ and 2π rad/s, except the few measurements close to the end disks (cf. figure 1*c*). The initial condition of solid-body rotation at $s = 0$ corresponds to $\langle\Omega\rangle/\Omega_i = 1$. Solid-body rotation during spin-down would result in uniform $\langle\Omega\rangle/\Omega_i$ values for fixed values of s (cf. (1)). The figure does not provide a uniform support for this assertion. It does, however, indicate that the core region may be looked upon as slowing down like a solid body, which is sufficient for the

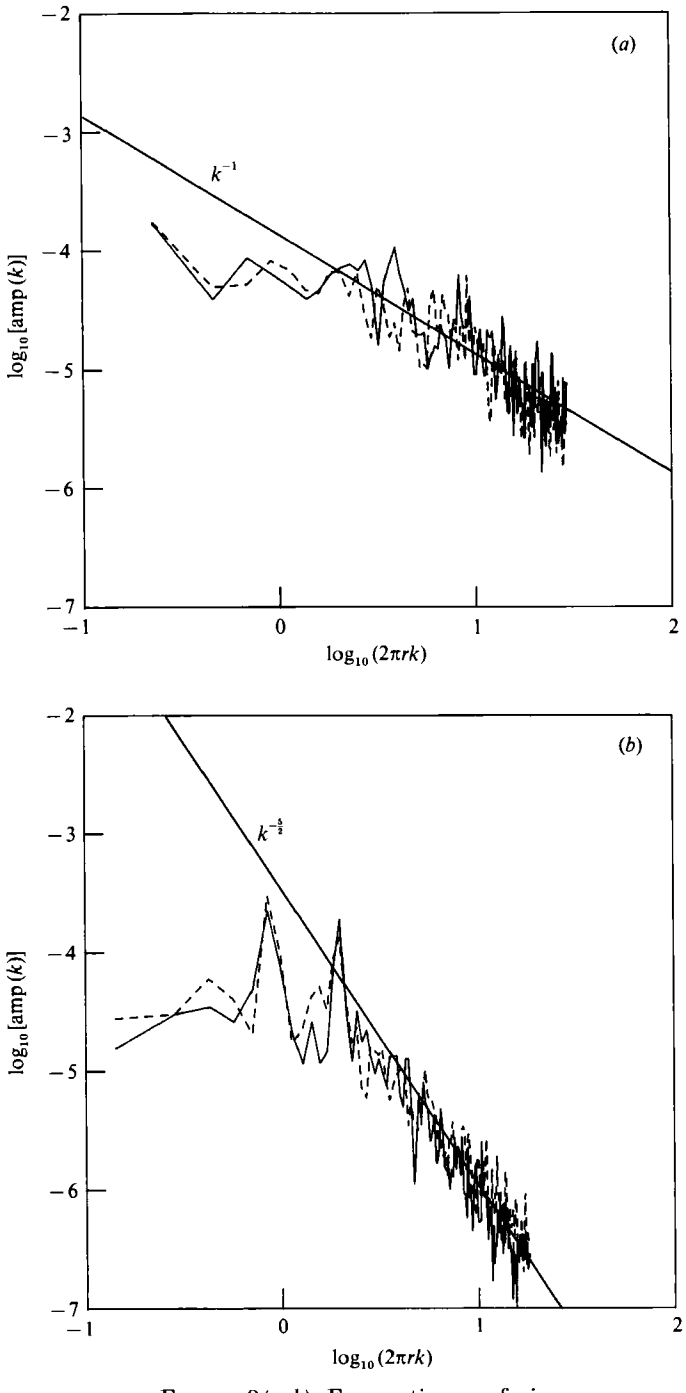

FIGURE 9(*a*, *b*). For caption see facing page.

acceptability of the model of (1) to obtain a timescale for the mean flow. The flow at its mature stage tends to a single vortex, as indicated by the profiles plotted for $s =$ 0.5, 1, and 1.8. The angular velocity $\langle \Omega(r/R, s) \rangle$ is higher at the centre and monotonically decreases outward. The data at $s = 0.5$ and 1.0 in the figure suggest a vortex, the core of which is in solid-body rotation.

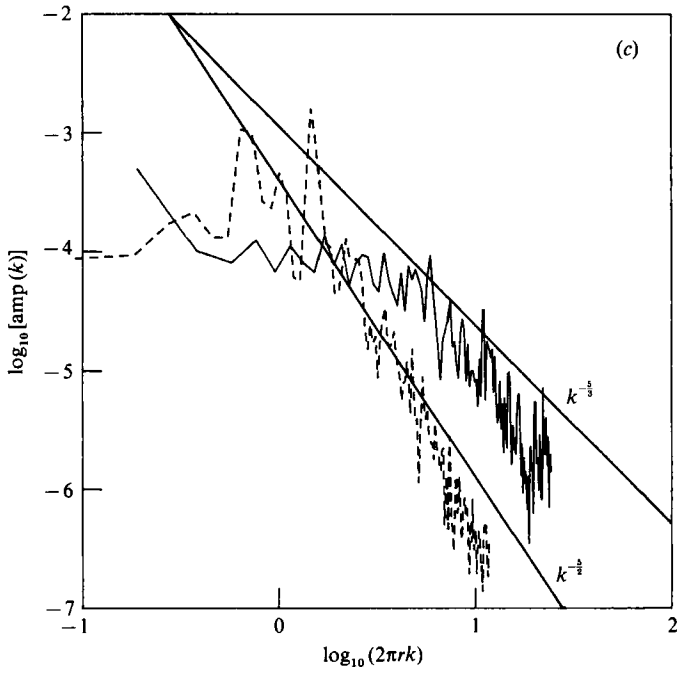

FIGURE 9. Autopower spectra of normalized data from the green (——) and blue (– – – – –) probes in various regions of the cylinder. The normalized data are divided into overlapping segments and windowed using Welch window (Press *et al.* 1986). (*a*) The flow over the concave wall. The corresponding correlations are shown in figure 8(*a*) above. Note the slow decay rate of about k^{-1}. (*b*) Flow in the core. The power spectra show a faster decay rate of about $k^{-\frac{5}{2}}$. The corresponding correlations are shown in figure 8(*b*). (*c*) Power spectra of simultaneous velocity traces in the core and buffer regions. Note the slower decay rate with the wavenumber in the buffer region. The lines $k^{-\frac{5}{2}}$ and $k^{-\frac{5}{3}}$ are drawn for reference. The flow corresponds to that in figure 8(*c*).

The photograph in figure 12 provides visual evidence for the development of a single vortex during the last phase of spin-down. The picture is taken in water at $t = 90$ s and $\Omega_1 = 9.77$ rad/s ($s = 1.8$ and $E_1 = 9 \times 10^{-6}$). It shows the footprint of a flow field, the local angular velocity of which is higher at the centre than at its perimeter, *that is*, a concentrated vortex. We base our conclusion on the observation that the flow at the centre shows a turbulent signature at the centre despite the calm, therefore presumably a laminar signature over most of the disk surface. The flow at the centre must have a substantially higher angular velocity to maintain an unstable signature against an incoming laminar secondary flow.

5. Conclusions

We have presented an experimental study of the flow in a closed cylindrical cavity during impulsive spin-down to rest. The flow exhibits instabilities at numerous levels. Our interest here is in the unsteady motion of the fluid outside the boundary layers. The nature of the experiment makes the use of conventional averaging techniques inordinately time consuming. We have circumvented this difficulty by making a spectral curve fit to the time-series velocity traces. The mean flow and the fluctuations are separated in the frequency domain. The spin-down timescale of the mean flow is sufficiently larger than that of the fluctuations to make the spectral curve fitting acceptable. The results are insensitive to the cutoff frequency used in

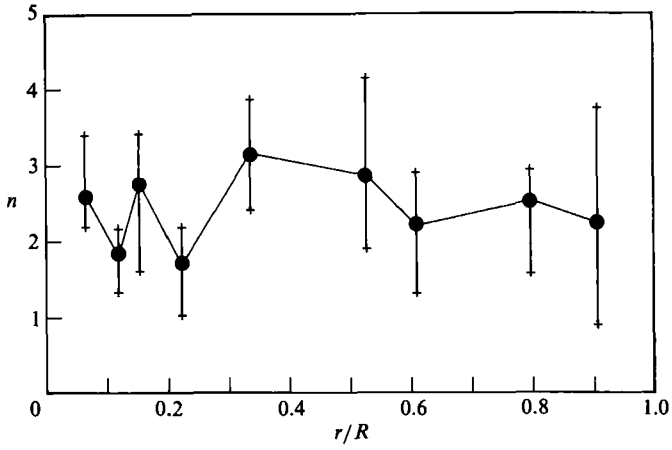

FIGURE 10. The exponent n of the curve fit k^{-n} to the power spectra of the scaled velocity traces for $2\pi rk > 2$. The vertical bars indicate the range of the scatter in n.

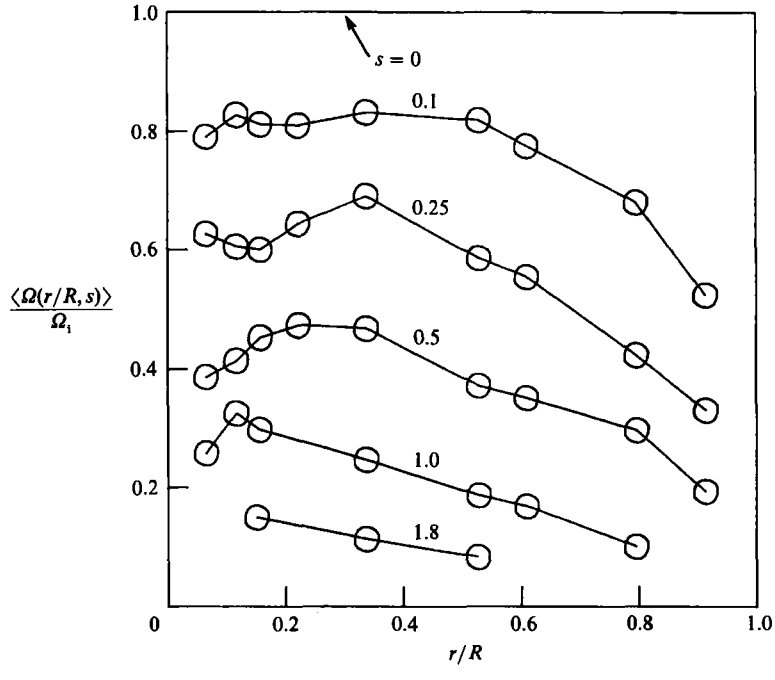

FIGURE 11. Instantaneous angular velocity profiles $\langle \Omega(r/R, s)\rangle/\Omega_1$ in the core during the final phase of spin-down to rest. Data points are averages over one-revolution segments of the velocity histories starting at dimensionless times $s = 0.1$, 0.25, 0.5, 1.0, and 1.8.

this method. The absolute amplitude of fluctuations decrease monotonically as the flow decelerates. When these fluctuations are scaled with the current mean velocity to obtain the relative fluctuations, we observe that their magnitudes remain approximately constant during the spin-down. Further, following Taylor's hypothesis, if the time is scaled with the current mean velocity, we note that the spectral content of these fluctuations remains similar during all phases of the flow. Some statistical properties of the flow are extracted from the velocity histories rescaled both in time and amplitude. The underlying assumption is the ergodicity of the flow; that is, one realization of the flow carries sufficient information to estimate

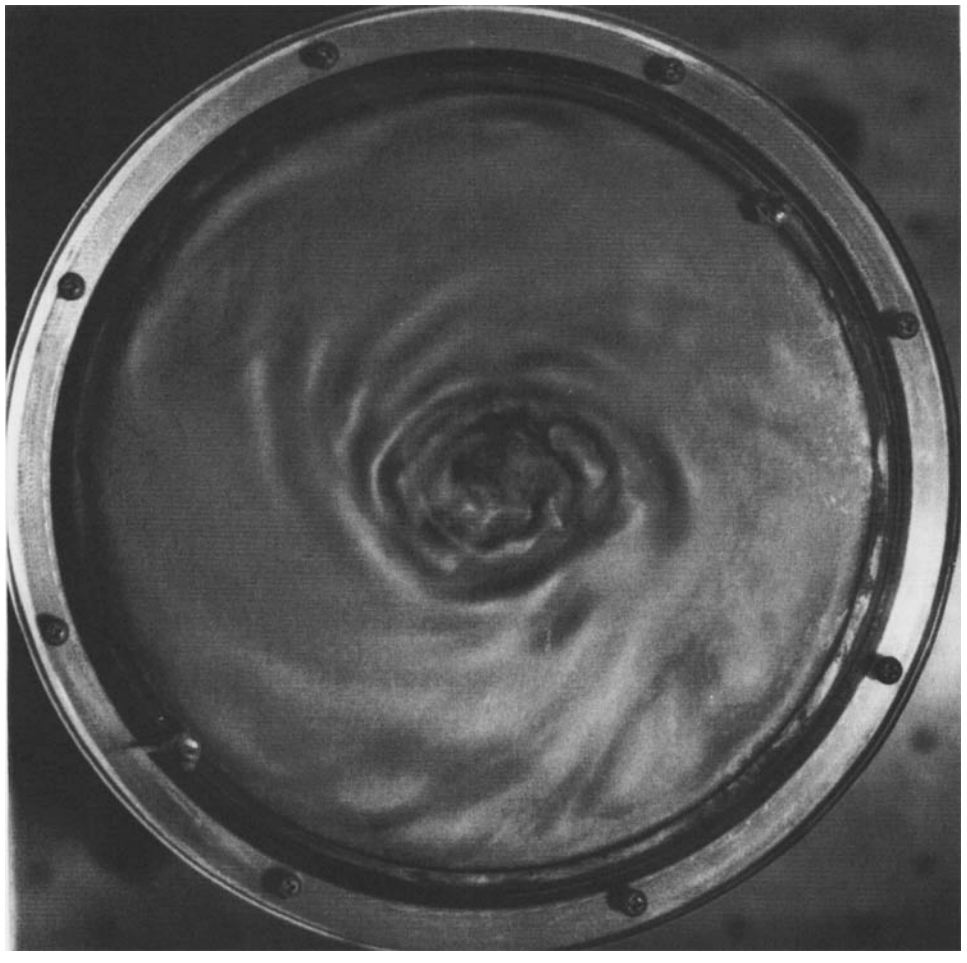

FIGURE 12. End view of cylinder at $t = 90$ s ($s = 1.8$, $E_i = \nu/\Omega R^2$ of 9×10^{-6} cf. figure 2). The flow tends to a single vortex, that is, higher angular velocity at the central zone as evidenced by a quiescent perimeter surrounding a wavy centre. note the contrast between the end view here and that in figure 2(*d*).

its statistics. This assumption is checked and substantiated by comparing the results obtained from successive realizations under similar conditions.

The conclusions derived are based on simultaneous azimuthal velocity measurements with two independent laser-Doppler velocity probes. The results are corroborated by flow visualization studies. The flow domain may be separated into distinct regions: a core that on average slows down like a solid body; the two turbulent Bödewadt layers over the disks which maintain the circulation within the cylinder; the concave wall where Taylor–Görtler vortices are the dominant feature; and a buffer region at the perimeter, between the core and the vortices over the concave wall. Our interest is in the core and the buffer regions. Strong vertical correlations at large separations during spin-down indicate a nearly two-dimensional structure. This is further substantiated by flow visualization experiments. The scaled fluctuation intensities suggest an r^{-1} behaviour in the core and are uniform away from the core through the buffer region but outside the region of Taylor–Görtler activity near the cylindrical wall. Power spectra in the cylinder suggest an $n = -2.6$

power dependence on the wavenumber k. Strong axial correlations, especially during the final phases of the flow, lead us to believe that the flow has a tendency to form a large single vortex as it matures. We consider this behaviour as evidence in favour of the hypothesis of vorticity expulsion from the core in a decelerating body of rotating fluid. We also speculate on the probable similarity of the spectral nature of the turbulence in the core to that in large eddies in turbulent shear flows. These large eddies are essentially concentrated vortical entities. More specifically, they are characterized by vorticity in a predominant direction. We expect that the turbulence characteristics are anisotropic. In particular, turbulence along the direction of predominant vorticity should decay faster than that in the transverse directions. The similarity to spin-down ought to be sought in the spectral contents of turbulence in those structures.

I thank Mr Mahboob Alam for his help during the experiments. This work was in part supported by NSF Grant MSM-8805892.

REFERENCES

BÖDEWADT 1940 Die Drehströmung über festem Grunde. *Z. Angew. Math. Mech.* **20**, 241–253.

BRETHERTON, F. P. & TURNER, J. S. 1968 On the mixing of angular momentum in a stirred rotating fluid. *J. Fluid Mech.* **32**, 449–464.

EUTENEUER, G.-A. 1972 Die Entwicklung von Längswirbeln in zeitlich anwachsenden Grenzschichten an konkaven Wänden. *Acta Mech.* **13**, 215–223.

GOUGH, D. O. & LYNDEN-BELL, D. 1968 Vorticity expulsion by turbulence: astrophysical implications of an Alka-Seltzer experiment. *J. Fluid Mech.* **32**, 437–447.

GREENSPAN, H. 1968 *The Theory of Rotating Fluids.* Cambridge University Press.

HOPFINGER, E. J., BROWAND, F. K. & GAGNE, Y. 1982 Turbulence and waves in a rotating tank. *J. Fluid Mech.* **125**, 505–534.

IBBETSON, A. & TRITTON, D. J. 1975 Experiments on turbulence in a rotating fluid. *J. Fluid Mech.* **68**, 639–672.

KRYMOV, V. A. & MANIN, D. YO. 1986 Spin-down of a fluid in a low cylinder at large Reynolds numbers. *Izv. Akad. Nauk SSSR: Mekh. Zhidk. Gaza No. 3*, 39–46 (English translation).

MATHIS, D. M. & NEITZEL, G. P. 1985 Experiments on impulsive spin-down to rest. *Phys. Fluids* **28**, 449–454.

MAXWORTHY, T., HOPFINGER, E. J. & REDEKOPP, L. G. 1985 Wave motions on vortex cores. *J. Fluid Mech.* **151**, 141–165.

NEITZEL, G. P. 1982 Marginal stability of impulsively initiated Couette flow and spin-decay. *Phys. Fluids* **25**, 226–232.

NEITZEL, G. P. & DAVIS, S. H. 1981 Centrifugal instabilities during spin-down to rest in finite cylinders. Numerical experiments. *J. Fluid Mech.* **102**, 329–352.

PRESS, W. H., FLANNERY, B. P., TEUKOLSKY, S. A. & VETTERLING 1986 *Numerical Recipes – The Art of Scientific Computing.* Cambridge University Press.

SAVAŞ, Ö. 1985 On flow visualization using reflective flakes. *J. Fluid Mech.* **152**, 235–248.

SAVAŞ, Ö. 1987 Stability of Bödewadt flow. *J. Fluid Mech.* **183**, 77–94.

SCORER, R. S. 1966 Origin of cyclones. *Sci. J.* **2** (3), 46–52.

WEDEMEYER, E. H. 1964 The unsteady flow within a spinning cylinder. *J. Fluid Mech.* **20**, 383–399.

WEIDMAN, P. D. 1976*a* On the spin-up and spin-down of a rotating fluid. Part 1. Extending the Wedemeyer model. *J. Fluid Mech.* **77**, 685–708.

WEIDMAN, P. D. 1976*b* On the spin-up and spin-down of a rotating fluid. Part 2. Measurements and stability. *J. Fluid Mech.* **77**, 709–735.